ORIGINAL ARTICLE

CIWEM Chartered Institution of Water and Environmental Management   Journal of Flood Risk Management   WILEY

Mixed debris interaction with obstacle array under extreme flood conditions

Piyali Chowdhury[1] | Indigo-Jaie Fredericks[1] | Jesus Castaño Alvarez[1] |
Matthew Clark[1] | Ravindra Jayaratne[2] | J. J. Wijetunge[3] | Alison Raby[1] |
Paul Taylor[4]

[1]Faculty of Science and Engineering, University of Plymouth, Plymouth, UK

[2]Department of Engineering & Construction, University of East London, London, UK

[3]Department of Civil Engineering, University of Peradeniya, Peradeniya, Sri Lanka

[4]Faculty of Engineering and Mathematical Sciences, The University of Western Australia, Perth, Western Australia, Australia

Correspondence
Piyali Chowdhury, Faculty of Science and Engineering, University of Plymouth, PL4 8AA, UK.
Email: piyali.chowdhury@cefas.gov.uk

Present address
Piyali Chowdhury, Centre for Environment, Fisheries and Aquaculture, Science, Lowestoft, UK.

Abstract

This investigation explores the interactions of different shaped debris with an array of obstacles under subcritical flow conditions, representative of a flood associated with a storm surge or tsunami. Panels, blocks and cylinders were used in a flow channel, as analogues for house panels, cars/containers and trees respectively, whilst some tests used a mix of debris. The backwater effect due to the blockage caused by the obstacles was most (least) significant for panels (cylinders). There was some evidence that smaller key log types and higher flow rates led to smaller dams. It was also evident that key logs formed at different depths depending on debris shape; debris shape also determined the vertical shape of the dam. Capture efficiency had a broadly negative (positive) correlation with the Froude number (permeability). Also, from video footage there were examples of the debris moving more quickly through partial dams. Finally, the drag force, deduced from only the water depths and the flow discharge, showed a clear relationship between drag force and Froude number, and a dependency of drag force on debris shape. There are some implications for the layout of building footprints in the inundation zones and the use of large, break-away panels.

KEYWORDS
coastal defence, debris flow, flood risk management plans

1 | INTRODUCTION

Global climate change is projected to increase the frequency and intensity of extreme events, such as cyclones, rainfall, and coastal flooding. It is also well-documented that there has been an increase in the compound flooding events arising due to the co-occurrence of heavy rainfall, high wind speeds and storm surges in low-lying coastal areas (Wahl et al., 2015; Zscheischler et al., 2018). In the Intergovernmental Panel on Climate Change (IPCC) report on the effect of climate change on coastal communities, one of the primary concerns is the increased vulnerability of coastal communities to extreme flooding events (IPCC, 2014). Furthermore, the devastation generated by recent major tsunami events, such as the 2004 Indian Ocean tsunami, the 2010 Chilean tsunami, and

the 2011 Tohoku tsunami have been responsible for catastrophic damage to coastal communities. Safety-critical defence infrastructure near the shoreline such as breakwaters, seawalls and coastal dikes were damaged and thousands of human lives faced unprecedented loss. The cause of damage has been observed to be due to the lack of structural capacity to sustain the extreme forces associated with the inundating tsunami bore (Esteban et al., 2015; Ghobarah et al., 2006). Several forensic engineering surveys have been performed following major flooding events (e.g., Kennedy et al., 2020; Mori et al., 2011).

A major factor that makes coastal flooding devastating is the transport of large quantities of debris (Naito et al., 2014; Nistor et al., 2017). Water-borne debris such as shipping containers, vehicles and wood logs are well known to exacerbate the structural damage on the built environment through the debris impact (collision) and damming loads (Park et al., 2021). Furthermore, the transport of debris can increase loading on structures and block important transport links, leaving the community at greater risk. Understanding the transport of debris and the characteristics of its motion is crucial because the debris impact depends on debris motion (Cinar et al., 2023). Due to the random nature of turbulent flood flows, debris motions are inherently random (Kasaei et al., 2021). Therefore, a better understanding of water-driven debris transport is essential to predict damages and losses on coastal communities (both economic and societal).

Debris, in the context of extreme wave events and this study, are objects of materials commonly found in coastal regions that are disturbed by the initial wave and then become entrained and transported in the direction of flow by subsequent waves. The additional loading caused by the entrained debris impacting a structure has been well documented under experimental conditions (Aghl et al., 2014; Ikeno et al., 2016). However, the additional loading caused by multiple trapped debris at an obstacle has been difficult to reproduce under experimental conditions due to the stochastic nature of debris transport (Stolle et al., 2017; Stolle et al., 2018). As the initial items of debris become trapped by the obstacles, referred to as a key log (Schmocker & Hager, 2013), other items of entrained debris can become trapped or lodged about the location of the key log, increasing the loading further. This build-up of debris items restricting the flow is referred to as a debris dam (Nistor et al., 2017). Rahman et al. (2022) conducted a series of model-scale experiments to elucidate the effects of a debris dam on local scouring and tsunami energy reduction on the landside of a coastal embankment model. A maximum reduction of 43.6%–48.8% of the total relative energy of the tsunami flow was found when eight rows of tsunami-borne debris were positioned (in experiment)/trapped (in reality) at the beginning of the embankment model toe, meaning the energy of the subsequent waves can be reduced if the trapping capability of the coastal forest is increased by the presence of multiple obstacles, that is, coastal plants. Having such environmentally friendly and effective debris countermeasure, such as a specially engineered coastal forest, could be a viable option. Furthermore, there is the potential to boost local economies due to the maintenance and the potential farming of the coastal forest (Tanaka & Onai, 2017). Post-event field investigations of disasters, including *The 1998 Papua New Guinea Tsunami* (Harada & Imamura, 2005), *The 2004 Indian Ocean Tsunami* (Danielsen et al., 2005) and *The 2011 Great East Japan Earthquake & Tsunami* (Naito et al., 2014; Raby et al., 2015) showed that structures behind dense vegetation displayed less damage than unsheltered structures (Tanaka & Onai, 2017). The usefulness of a coastal forest or mangrove as a mitigation for a debris-laden tsunami bore has been discussed (e.g., Danielsen et al., 2005; Harada & Imamura, 2005; Tanaka & Onai, 2017). However, due to the stochastic characteristics of debris transport and the difficulty of scaling properties, such as the buoyancy and stiffness, experimental research has been limited to simplified models, with most observations coming from field investigations (Nistor et al., 2017).

In this study, the interactions of different shaped debris with an array of obstacles (that mimics a coastal forest) under subcritical flow conditions were explored through laboratory-based experiments. Investigations were carried out to learn how different debris types interact with an array of obstacles, not previously considered. Backwater effect caused by various types of debris and debris dam formation during coastal flooding were also explored. Panels, blocks and cylinders were used (individually and mixed) in a flow channel, as analogues for house panels, cars/containers and trees, respectively. Relationship between the type of debris dam formation and the layout of building footprints in the inundation zones were also investigated.

Section 2 describes the experimental setup, Section 3 presents the key results and discussions on backwater rise, dam formation, capture efficiency, array affects and drag force. Section 4 summarises the findings and suggests recommendations.

2 | METHODOLOGY

2.1 | Flume set-up

Experiments were carried out in the 35 m long Sediment Flume in the COAST Laboratory at the University of

FIGURE 1 Schematic drawings of the Setup B arrangement.
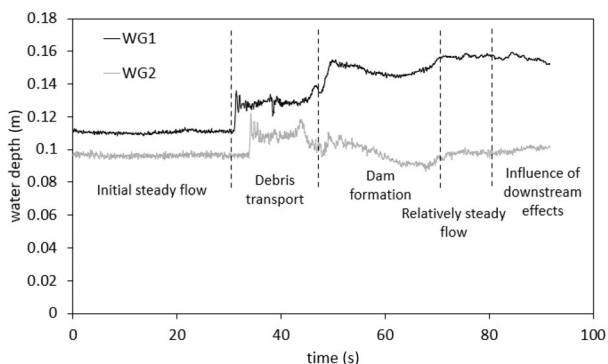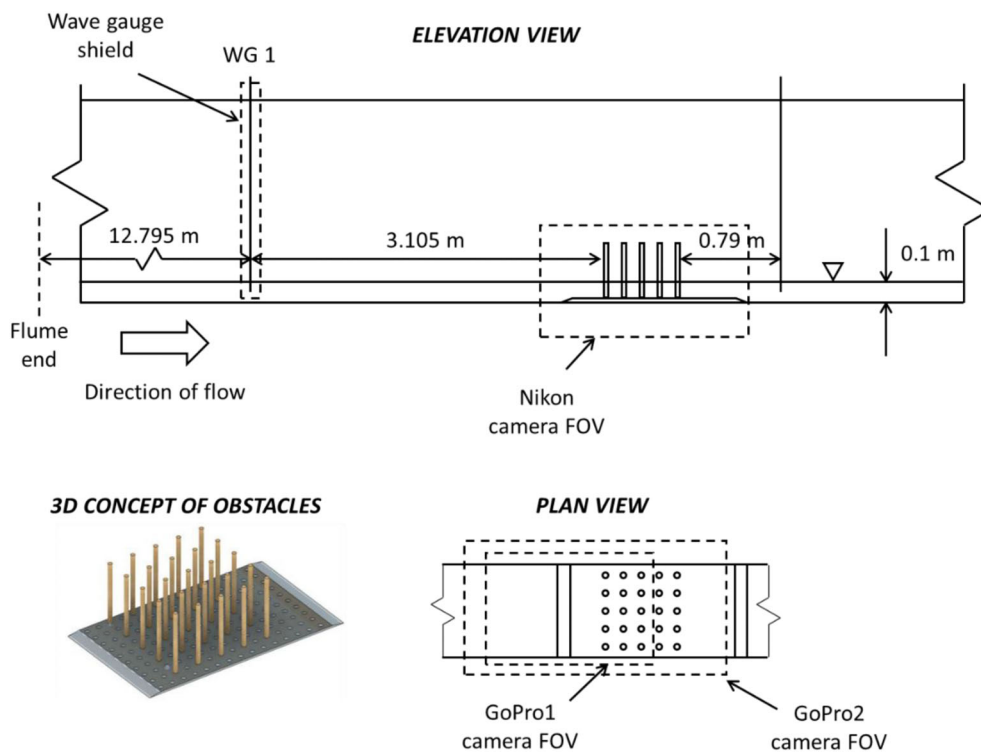
FIGURE 2 Wave gauge time histories from Repeat 3—panel debris test.

Plymouth. The 35 m long Sediment Flume has a working section of 0.6 m wide and a maximum still water depth of 0.8 m. The obstacles comprised a 5 × 5 rectilinear array of 20 mm diameter wooden dowels inserted into a 10 mm board fixed to the flume bed. The dowels were of sufficient height to be only partially submerged and the base board had tapered ends to reduce disturbance of the flow. Two tranches of tests, Setup A and Setup B, were undertaken. Figure 1 shows schematic drawings of the Setup B general layout. In Setup A there were slightly different placements of the wave gauges (WGs), with WG1 just 1 m upstream of the obstacles, and WG2 1.4 m downstream of the obstacles. The still water depth was 0.1 m for both setups. Assuming a geometric scale of 40:1 gives an equivalent full-scale water depth of 4 m, not unreasonable in many large tsunamis and storm surges.

Two resistance-type wave gauges (WG1 and WG2) were used for both experimental setups, acquiring data at 128 Hz. Three video cameras were used: (a) a side-view Nikon camera and (b) two overhead GoPros.

Typical surface elevation time histories obtained from WG1 and WG2 are shown in Figure 2. The gauges suffered from a little high-frequency noise. However, filtering was not necessary as most of the data was averaged over a reasonable time duration. Up to 30 s in Figure 2, before debris is introduced, there are steady flow conditions. The upstream water depth is clearly higher than the downstream, due to a back-water effect caused by the fixed obstacles (see Section 3.1). Shortly after 30 s, the release mechanism is activated and debris is introduced into the flow, upstream of the obstacles and the wave gauges. This results in a surge being recorded by both gauges between about 30 and 45 s. A dam is then formed over a period of time; here the backwater effect increases further, and the downstream depth is reduced. After about 70 s, there is a period of relatively steady flow again. However, by about 80 s, the debris that passed through the obstacles without being trapped is reflected from the end of the flume and begins to influence the upstream locations. Water depths without debris were determined from the initial steady flow period, and with debris during the relatively steady flow period. These periods of time were different depending on the time at which debris was introduced after data acquisition started, and what debris type was used, which

TABLE 1 Flow characteristics.

		Upstream			Downstream		
	Q (m³/s)	u_1 (m)	h_1 (m/s)	Fr_1	u_2 (m)	h_2 (m/s)	Fr_2
Setup A	0.0227	0.280	0.14	0.24	0.29	0.13	0.25
	0.0400	0.380	0.18	0.29	0.40	0.17	0.31
	0.0585	0.510	0.19	0.37	0.55	0.18	0.42
Setup B	0.0329	0.492	0.11	0.47	0.55	0.10	0.556

governed how quickly a dam formed. Therefore, each set of data was manually checked, cross-referencing with the videos.

Scaling for these experiments relies on appropriately scaling the significant forces, here the gravity and viscous forces. Scaling of gravity forces is achieved by Froude scaling, and viscous forces in the fluid boundary layer are assumed to be small, because the experiments are undertaken in the fully turbulent regime with Reynolds numbers in the range 3×10^5 to 6×10^5.

The Froude number, Fr, was calculated according to:

$$Fr = \frac{u}{\sqrt{gh}}, \tag{1}$$

where u is velocity (ms⁻¹), g is acceleration due to gravity (9.81 ms⁻²) and h is water depth (m). Fr values are given in Table 1, where the subscripts 1 and 2 refer to upstream and downstream conditions, respectively. A Valeport Model 002 flow meter was used to determine the upstream velocities. It was situated along the flume centreline and at a depth that ensured it was fully submerged despite the rather bulky impeller (50 mm diameter). In preparatory tests, five equally spaced velocity measurements across the width of the channel revealed a variation about the mean velocity of just −3% to 7%, since the flow was fully turbulent. For the variation of mean flow with depth at the centreline, the 1/7th power law for the boundary layer profile is assumed to be relatively flat over the entire depth for a smooth flume well-upstream of any obstructions. Therefore, point measurements at the centreline were assumed to be representative of the average velocity across the section for all tests. Downstream velocities were inferred from the upstream velocities and the measured water depths (using the principle of conservation of flow, i.e., $u_1 h_1 = u_2 h_2$).

Upstream of the obstacle field, Fr indicated that the flow regime was sub-critical ($Fr < 1$) for both Setup A and B, and remained sub-critical downstream, despite the reduction in water depth. These Froude numbers are slightly lower than used by other investigators; for example, Schmocker and Hager (2013) considered Froude numbers between 0.5 and 1.5.

2.2 | Debris mixes

The two different setups (A and B) had different debris mixes:

- Setup A (one debris mix and three different flow rates) and
- Setup B (several debris mixes including sole debris types with one flow rate)

In actual inundation events, debris flow would normally comprise different shaped objects with a variety of roughness, but it is instructive to see the behaviour of simple plane objects, for example, blocks or cylinders only. The compositions of the various debris shapes are provided in Tables 2 and 3. The debris dimensions were approximated from a 1:40 length scale of standard debris objects, historically found in debris dams during extreme wave inundation events. For example, the blocks (150 mm × 50 mm × 50 mm) are roughly equivalent to standard 20 ft storage containers (6058 mm × 2352 mm × 2352 mm), the larger panels (100 mm × 100 mm × 3 mm) scaled by 40 give a full-scale dimensions of 4 m × 4 m × 0.12 m, appropriate in size to wooden frames in a house, and the longest cylinders (15 mm diameter × 310 mm length) scaled up by 40, represent tree trunks with a diameter of 600 mm and length 12.4 m. The sizes are similar to the debris used in the experiments by Stolle et al. (2018). Setup B tests were about 37% the total volume of the Setup A debris. Table 3 also indicates the size of the debris (W/D, width; L, length; T, thickness).

To ensure repeatable debris incorporation, a debris 'dam break' system was designed (Figure 3). The gate design required it to be capable of resisting the additional loading caused by the build-up of debris during the pump's start-up phase and only release when triggered. The gate at the bottom of the mechanism holds back the submerged debris. The release mechanism operates by dropping the weight connected via a pulley (Figure 3b) onto the platform, which rotates the gate around the hinge. Releasing the debris in this way ensures that no surface waves are generated which would travel both

TABLE 2 Debris geometries for Setup A.

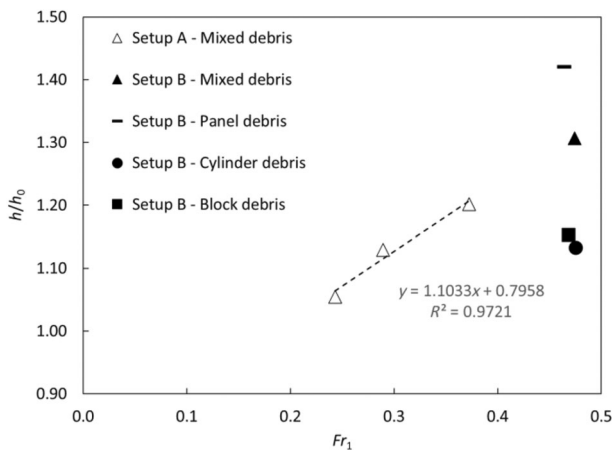| Debris type	ID	W or D (mm)	L (mm)	T (mm)	Indiv. A (mm^2)	Indiv. vol (mm^3)	Nos.	Vol. (dm^3)
Panels	P1	30	30	3	900	2700	30	0.08
	P2	100	50	3	5000	15000	30	0.45
	P3	100	100	3	10000	30000	20	0.60
Blocks cylinders	B	150	50	50	7500	375000	20	7.50
	C1	15	70	—	1050	12370	30	0.37
	C2	15	160	—	2400	28274	30	0.85
	C3	15	310	—	4650	54782	20	1.10
Total volume (dm^3)								10.95

FIGURE 4 Relative backwater rise as a function of upstream Froude number for Setup A and B tests.

upstream and downstream given the sub-critical flow regime. The mechanism incorporates a platform strong enough to stand on during the loading phase. The debris upstream of the gate was organised by type, then divided into four groups and distributed evenly between each of the four 'quadrants' of the loading area.

3 | RESULTS AND DISCUSSION

3.1 | Backwater rise

To demonstrate the effect of obstacles on the flow depth over a range of flow conditions, the dimensionless backwater rise h_1/h_0 is considered, where h_0 is the approach flow depth without obstructions (m). This is plotted in Figure 4 as a function of the Froude number for all tests. For Setup A, there appears to be a fairly strong correlation between backwater rise and Fr with a best-line fit of

$$\frac{h_1}{h_0} = 1.9\,Fr + 1.4. \tag{2}$$

A similar trend is also found by Schmocker and Hager (2013):

$$\frac{h_1}{h_0} = 1.1\,Fr + 0.8. \tag{3}$$

However, their gradient is more gentle than for these present tests; this may be due to the larger Froude numbers that they considered (0.5–1.5). Setup B tests were all conducted at the same flow rate, but slight differences in the initial surface elevations give a small spread in Fr. Despite their similar Froude number values, the backwater rise varies considerably for the different debris types: the greatest values are caused by the panel debris, followed by the mixed debris, the blocks and finally the cylinder. The Setup B mixed debris tests caused greater relative backwater rise than the equivalent Setup A tests, despite the much smaller volume of debris, presumably because of the larger Froude number values.

3.2 | Dam formation

For Setup A, the physical order in which the different debris shapes were released was uncontrolled, which contributed to a range of dam formation characteristics. One notable, qualitative, finding was that whenever the smaller debris (cylindrical pole in Figure 5a,b) formed the key log, the debris was consistently captured with a lower capture rate (Section 3.3), whereas whenever the larger debris formed the key log (panel in Figure 5c,d), a more stable debris dam was formed, resulting in a greater capture rate.

The dam formation was complicated by the fact that some of the items of debris are not large enough to span the distance between obstacles. Therefore, more than one key log was required to form a dam across the entire width of the flume, with each gap between obstacles

TABLE 3 Debris geometries for Setup B.

| Debris type	ID	W or D (mm)	L (mm)	T (mm)	Indiv. A (mm²)	Indiv. Vol (mm³)	Mixed group nos.	Mixed group vol. (dm³)	Panel group nos.	Panel group vol. (dm³)	Cylinder group nos.	Cylinder group vol. (dm³)	Block group nos.	Block group vol. (dm³)
Panels	p1	50	120	4.6	6000	27,600	8	0.22	25	0.69	—	—	—	—
	p2	70	140	3.8	9800	37,240	3	0.11	10	0.37	—	—	—	—
	p3	80	100	3.6	8000	28,800	3	0.09	9	0.26	—	—	—	—
	p4	100	120	3.6	12,000	43,200	2	0.09	6	0.26	—	—	—	—
	p5	95	64	4.8	6080	29,184	3	0.09	9	0.26	—	—	—	—
	p6	75	64	4.8	4800	23,040	5	0.12	14	0.32	—	—	—	—
	p7	71	120	3	8520	25,560	21	0.54	64	1.64	—	—	—	—
Blocks	b	43	100	37	4300	159,100	9	1.43	—	—	—	—	27	4.30
Cylinders	c1	20	80	—	1600	25,133	9	0.23	—	—	28	0.70	—	—
	c2	20	160	—	3200	50,265	8	0.40	—	—	24	1.21	—	—
	c3	20	310	—	6200	97,389	8	0.78	—	—	24	2.34	—	—
Total volume (dm³)								4.08		3.80		4.25		4.30

capable of having a key log. An overhead and side view of the dam formation for mixed group debris is shown in Appendix A.

Despite the rather random introduction of debris shapes into the flow, Setup A did show evidence of the dependence of the dam volume on the flow severity. Generally, the length of the dam in the flow direction reduced for increasing Froude numbers. This is shown qualitatively and quantitatively in Figures 6 and 7, respectively. Figure 6 is an overhead view of Setup A tests, showing representative dams for each of the three flow rates. The volumes in Figure 7 were estimated by identifying the trapped debris, and multiplying each one by its respective volume. Determining the exact composition of the dam from video footage was a tedious task, requiring the counting of debris types that passed into the frame using slow video frame rates. It was not possible to alternatively count debris from the video after the dam formed, as there was significant overlapping between pieces.

In Setup B, the debris items were placed in identical arrangement for each of the repeat tests as described in Section 2.1. For the cylindrical debris, the process of accumulation was the same as that reported by Schmocker and Hager (2013) with the key log forming at the surface, but subsequent debris forcing it toward the bed of the flume. However, for the panel debris this process was quite different; due to the larger possible contact area between the panel debris and the obstacles, the potential to become trapped about its centre of mass increased. A panel key log occurred at a wider variety of depths, compared with the cylindrical debris. For the mixed group, the smaller cylindrical debris, the panel and the block debris reached the obstacles first, followed by the majority of the larger cylindrical debris. This was due to the interaction between the large cylindrical debris and the upstream wave gauge, which acted to break up the conglomerate of debris formed at the debris release. Figure 8 shows examples of fully formed dams for the four debris groups. The examples show how the length of the debris dam along the flow direction decreases with water depth, with the majority of trapping happening at the water surface. Due to the larger buoyancy force of the block debris, subsequent debris items were not strong enough to push the key log toward the bed of the flume, as also seen by Pasha and Tanaka (2020) and Stolle et al. (2018). The panel group resulted in the most compact and evenly distributed dam of all the groups, in both the horizontal and vertical directions.

For interest, Figure A1 in the appendices shows 0.5 s intervals of dam formation for the mixed group.

FIGURE 3 Setup B debris release mechanism (a) conceptual drawing (b) laboratory model.
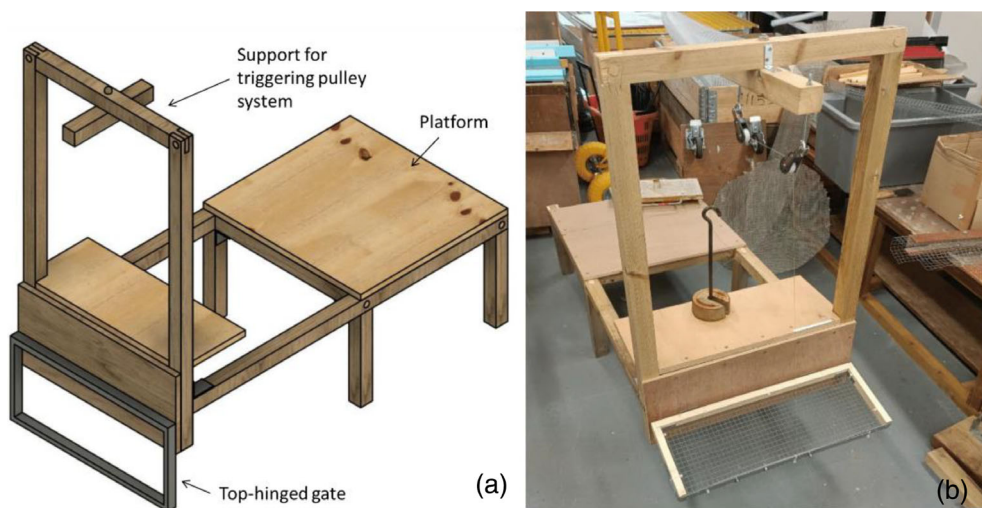
FIGURE 5 Two examples of key logs: (a) a cylinder leading to a modest dam shown in (b); (c) a panel leading to a larger dam formation as shown in (d).
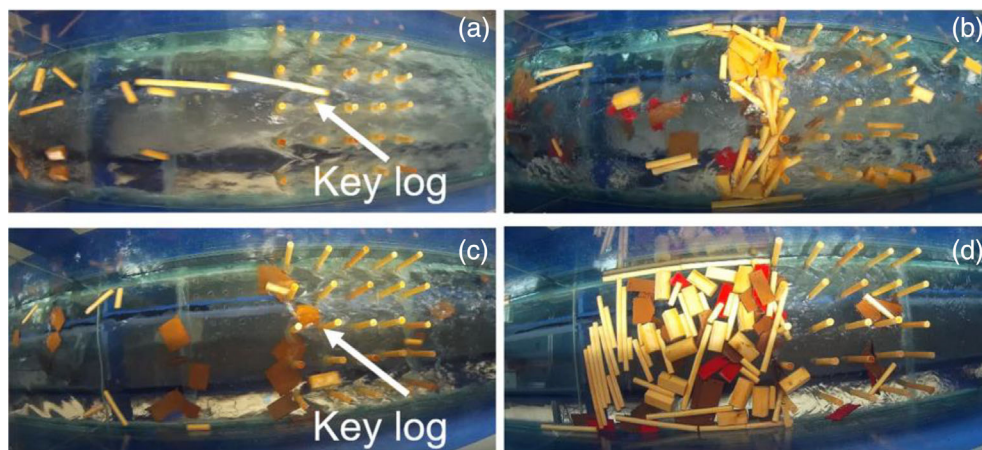
3.3 | Capture efficiency

Capture efficiency (C_e) is the ratio of the number of released objects trapped by the obstacles, compared with the total number of objects. For Setup A, the capture efficiency of the different debris types was determined from the video footage. Figure 9 shows the capture efficiencies of each repeat test of each debris type, as a function of Froude number. This reveals how the debris trapped by the obstacles varies with the flow severity.

The degree of repeatability in Figure 9a–c was generally better for the lowest flow rate ($v = 0.28$ m/s), where the larger dams are also formed (Section 3.2). Repeatability was clearly affected by the random manner in which the debris types were introduced. Some of the panel types show a consistent reduction in capture efficiency with increasing flow rate (the medium and large dowels, and the blocks), agreeing with Stolle et al. (2017), but some (small dowels and all panels) show an initial reduction in capture efficiency with flow rate, followed by a slight

increase again. An unwanted experimental effect, was that a considerable amount of panels, especially small ones and at lower speeds, stuck to the bottom of the flume and were not dragged by the flow; they therefore did not reach the obstacle array, affecting the capture efficiency.

To investigate how the relative size of the debris compared with the obstacles, affects the capture efficiency in the more repeatable Setup B, a permeability ratio (P) is defined as (ratio of individual debris cross-sectional area to square of gap between obstacles)

$$P = A_p/S^2, \qquad (4)$$

where A_p is the debris plan area (determined from the largest cross-sectional area) and S is the gap between obstacles, designed as 0.1 m for the current experiments.

For Setup B, Figure 10 shows the correlation between the capture efficiency and the permeability ratio for repeat tests of the different debris groups. Data inferred
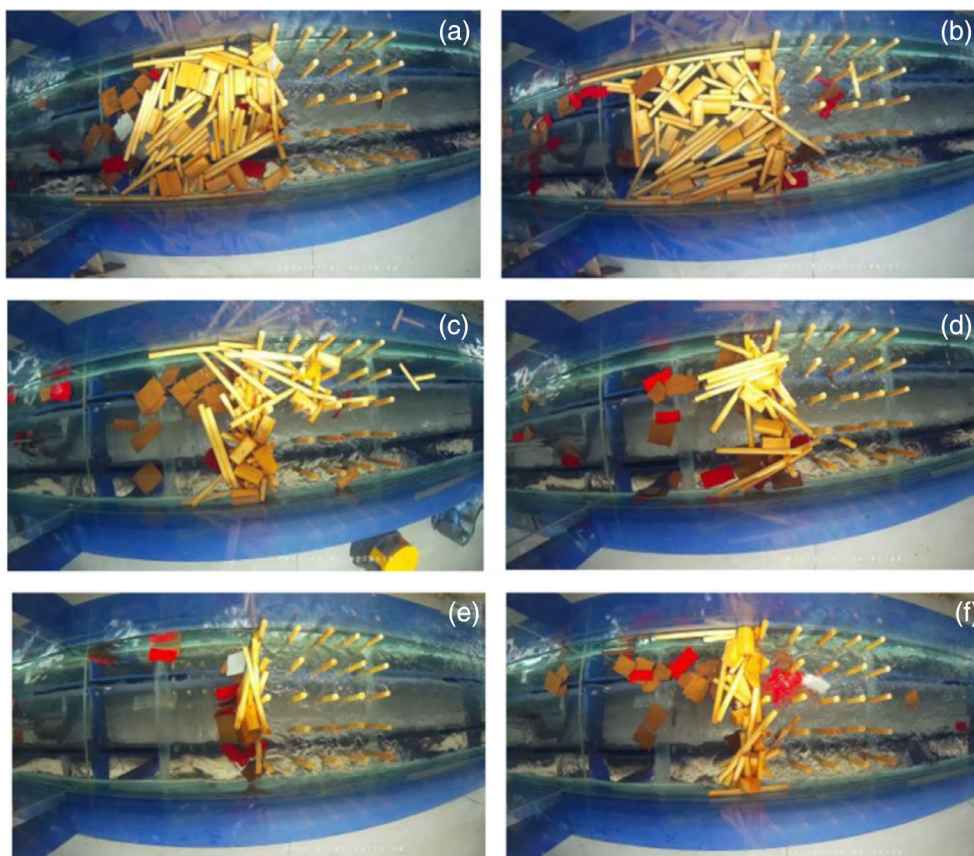
FIGURE 6 Dam lengths for three different flow rates, two representative examples of each: (a,b) $u = 0.28$ m/s, (c,d) 0.38 m/s, (e,f) 0.51 m/s.
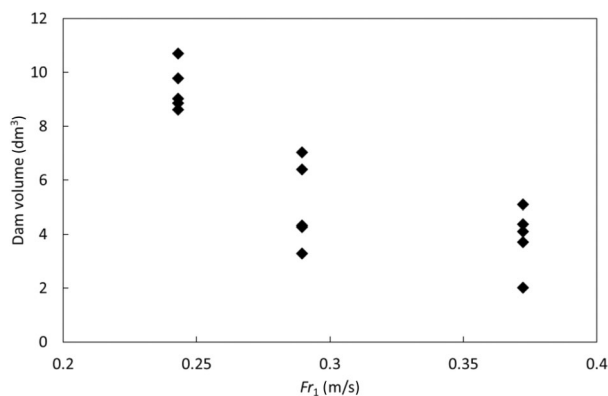

FIGURE 7 Dam volume as a function of Froude number for Setup A.

As the permeability tends to 1, the cross-sectional area becomes comparable to the space between obstacles. However, for shapes that are elongated (e.g., the cylinders), the plan area does not provide a good indication of the likelihood of obstruction. The capture efficiencies of all the cylinders lies below the trend line. For some unknown reason, the Stolle cylinder has a relatively high capture efficiency compared with the ones from the present tests, despite having an even greater length-to-diameter ratio (24) compared with the present tests (15.5). The debris with the highest degree of scatter in the capture efficiency are the blocks which vary between <0.1 and >0.8. One difference is that block debris travel with greater momentum than other smaller debris. Videos show how the debris dam formed by blocks can on occasion be quickly broken up and disturbed by subsequent blocks travelling downstream. So, the variability in the capture efficiency for such debris may just represent the range of possible dam behaviours. More than five repetitions for each test would be valuable to give greater confidence of the correlation between capture efficiency and permeability ratio. Capture efficiency had a broadly negative correlation with the Froude number and a broadly positive correlation with permeability (ratio of individual debris cross-sectional area to square of gap between obstacles) but with a high degree of scatter.

from Stolle et al. (2017) for the three debris types are also included.

There is a weakly increasing trend of capture efficiency with the permeability ratio, determined using the mean values of C_e as follows:
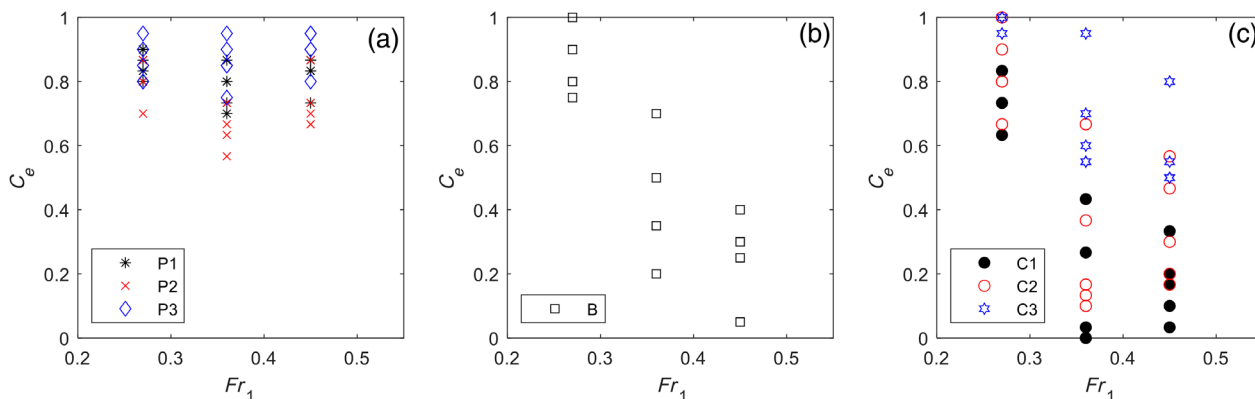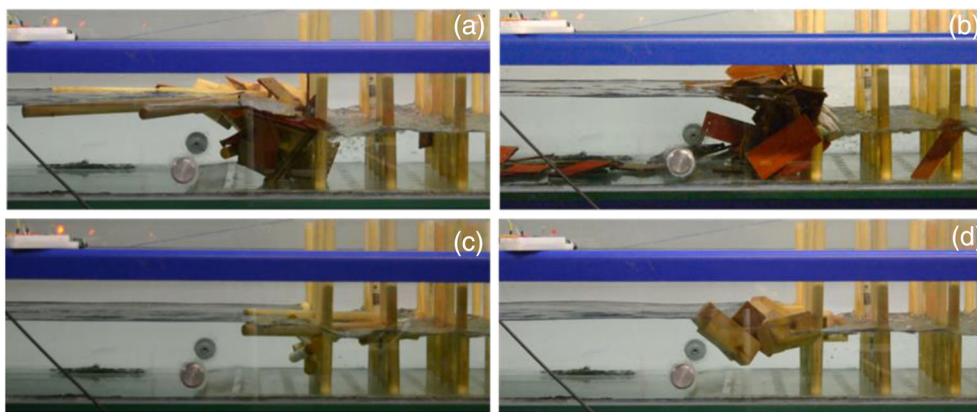
$$C_e = -0.376P^2 + 1.033P + 0.2565. \qquad (5)$$

The trend is plausible as the larger the debris plan area, the more likely it is to get caught by the obstacles.

FIGURE 8 Typical dam formation for the four debris group types in Setup B: (a) mixed, (b) panels, (c) cylinders and (d) blocks. The light trigger top left was used to match the video footage with the wave gauge data.
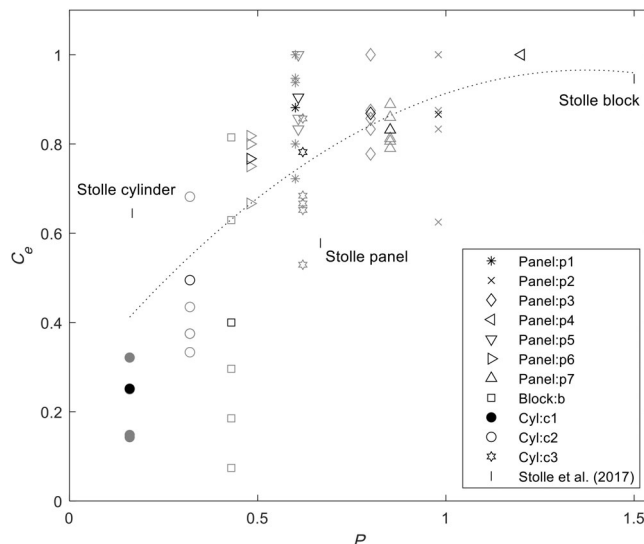

FIGURE 9 Capture efficiencies as a function of upstream Froude number: (a) panels, (b) blocks and (c) cylinders.

3.4 | Array effects

Most previous investigations have only considered the hydrodynamics of debris flow around a single row of obstacles, except for Goseberg et al. (2016) who considered two rows. Here, we can see how debris transit is affected by the presence of a two-dimensional plan array of obstacles. This is a more realistic scenario that simulates a tree plantation or regular array of buildings and streets. Qualitatively, for Setup B, it was observed that the presence of a dam (RHS of Figure 11) caused debris to move much more quickly than in the absence of a dam (LHS of Figure 11) for the same flow rate. Qualitatively, for Setup B, it was observed that the presence of a dam caused debris to be accelerated through gaps in the dam, as indicated in Figure 11.

In Figure 11 the images on the left-hand side (LHS) show the transit of a small cylinder, highlighted in the frames by a yellow circle, travelling unimpeded through the array, in the absence of any dam. On the right-hand side (RHS) the same size cylinder is shown to move much more rapidly along the same 'avenue' in the situation where a dam had formed across a large proportion of the

FIGURE 10 Capture efficiency as a function of permeability ratio for each debris type, where dark/solid symbols represent the mean values, calculated from individual values shown in feint, with a polynomial trend line plotted through the mean values. Results from the three debris shapes used by Stolle et al. (2017) are also included.
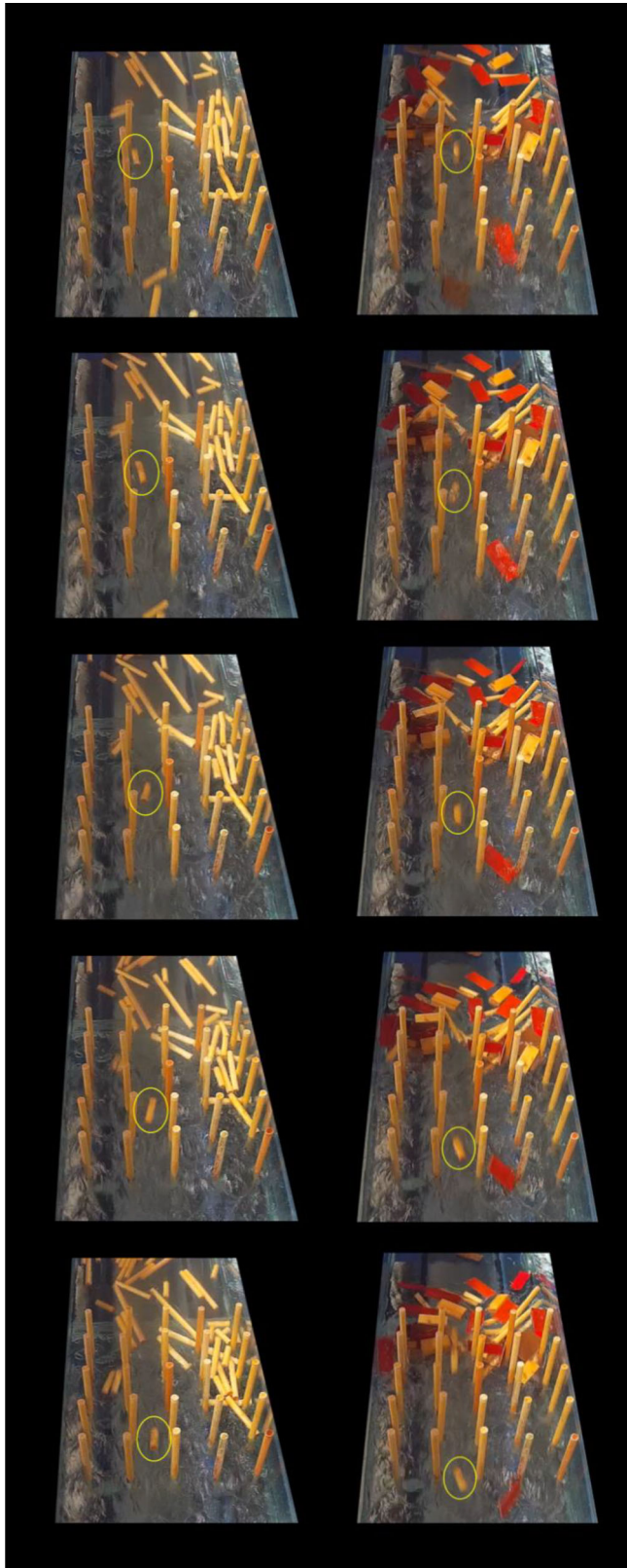
FIGURE 11 Video frames selected at 1/6 s intervals to track the motion of a small cylinder through obstacle array: LHS (no dam) and RHS (with dam).

flume. It is not unexpected that with the partial dam the cylinder would move faster (from a conservation of flow principle), but it does highlight a potential hazard

where debris can be accelerated around partial dams. This finding may be related to the observations by Bocchiola et al. (2008) that dowels travelled further down a flume when there is congested transport.

3.5 | Drag force

The drag force, F_D (N), exerted by the obstacles and trapped debris on the flow, as illustrated in Figure 12, can be determined from the steady-state momentum equation as follows (Massey & Ward-Smith, 1998)

$$\frac{\rho g h_1^2}{2} - F_D - \frac{\rho g h_2^2}{2} = \rho Q (u_2 - u_1), \qquad (6)$$

where ρ is the density of water (1000 kg/m³), g is the acceleration due to gravity (9.81 m/s²), h_1 and h_2 are the upstream and downstream water depths (m), respectively, Q is the discharge flow rate (m³/s), and u_1 and u_2 are the upstream and downstream velocities (m/s) respectively.

Rearranging Equation (6) gives

$$F_D = \frac{\rho g}{2} \left(h_1^2 - h_2^2 \right) + \rho Q (u_2 - u_1). \qquad (7)$$

The flow discharge can be defined as $Q = Au = bhu$, where A is the cross-sectional area of the flow (m²), u is the mean velocity (m/s) and b is the width of the flume (m). We assume that our measured velocities approximate the mean velocity of the flow (as described in Section 2.1), that is, the momentum coefficient = 1. Furthermore, if continuity of flow is assumed, that is, the upstream and downstream discharges are the same, the respective velocities can be written as

$$u_1 = \frac{Q}{b h_1}, \qquad (8)$$

and

$$u_2 = \frac{Q}{b h_2}. \qquad (9)$$

Making these velocity substitutions into Equation (7) yields

$$F_D = \frac{\rho g}{2} \left(h_1^2 - h_2^2 \right) + \frac{\rho Q^2}{b} \left(\frac{1}{h_1} - \frac{1}{h_2} \right). \qquad (10)$$

Hence, with a knowledge of the discharge, and the upstream and downstream water depths, the drag force

FIGURE 12 Definition sketch indicating the flow and resulting drag force on the trapped debris obstacles.
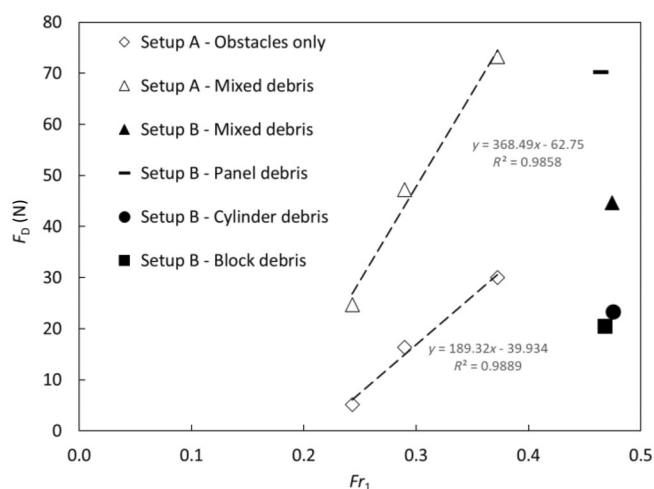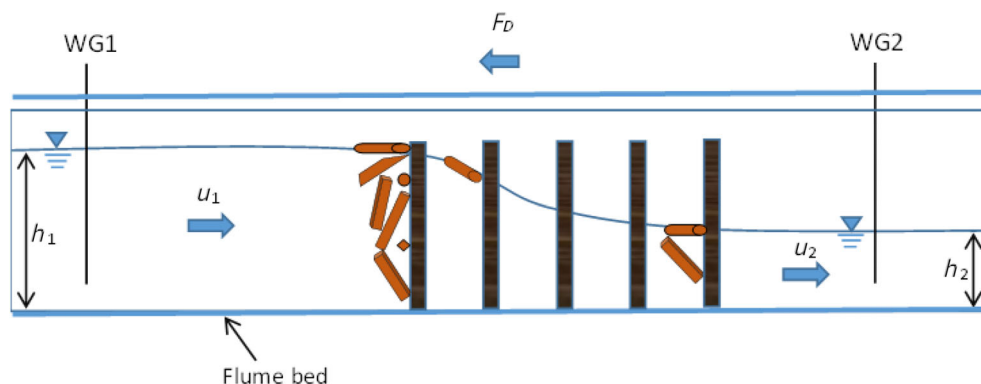

FIGURE 13 Drag force as a function of upstream Froude number for Setup A and B tests.

can be computed, but only when the flow is steady. We take this to be immediately after the dam is established.

Figure 13 indicates how the flow severity affects the estimated drag force on the trapped debris and obstacles, by plotting F_D against Fr_1. For Setup A, drag forces due to the obstacles only (for tests with no debris) and the mixed debris plus obstacles are plotted. For both the obstacles and the debris plus obstacles, there is a roughly linear trend between the drag force and the Froude number; this is very similar to the dependence of dimensionless backwater on Froude number shown in Figure 4. For Setup B, only predictions from obstacles plus debris are plotted. All the tests were done with very similar Froude numbers, but there is a large variation in the inferred drag force depending on the debris type. This is again very similar to the backwater versus Froude number findings, with the highest drag forces on the panel debris, then the mixed debris, and the cylinders and blocks experiencing the least force. The drag force is lower for the blocks than the cylinders, contrary to the findings for backwater rise; this small difference may be due to the fact that only two block tests were undertaken,

and the noise levels on the downstream wave gauge for those tests were particularly high. The similarity of the drag force and the backwater rise trends is not particularly surprising as they both have a strong dependence of the difference between the upstream and downstream water levels. For Setup B, drag forces are not as high as one might expect, with their higher Fr. However as shown in Figure 9, the capture efficiency of the cylinders and blocks tends to decrease with increasing Froude number so there will be fewer obstacles to block the flow hence the drag force would be relatively lower.

Figure 14 shows how the drag force varies of a function of both the maximum possible area of the items of debris making up the dam (using all the trapped debris and each of their respective maximum cross-sectional areas), and the actual total volume of the debris in the dam. There is a relatively linear relationship between the drag force and the areas of trapped debris, with the blocks causing least drag and the panels most. However, the debris had considerable overlaps so this area is a fairly unrealistic measure. When volume is considered, the trend is not as clear. This is due in large part to the block debris, which has the largest trapped volume of all the debris but creates the smallest drag force. This is likely to be due to their relatively high volume to area compared with the other objects.

To determine whether the drag forces determined in this simple setup are reasonable, comparisons are made to estimations from Macabuag et al. (2018). They compared predicted hydrodynamic loads from a variety of design codes as a function of inundation depth, for a case study of a uniform 1:20 beach with a tsunami run-up of 15 m, assuming buildings of urban density. The present experiments assume a geometric length scale of 40:1 in a flume of width 0.6 m. Knowing that with Froude scaling, forces scale according to the length scale cubed (Hughes, 1993), the minimum and maximum full-scale drag forces from the experiments (34.2 and 122.0 N/m, respectively) are equivalent to 55 and 195 kN/m, respectively, at full-scale. Macabuag et al.'s (2018) graph
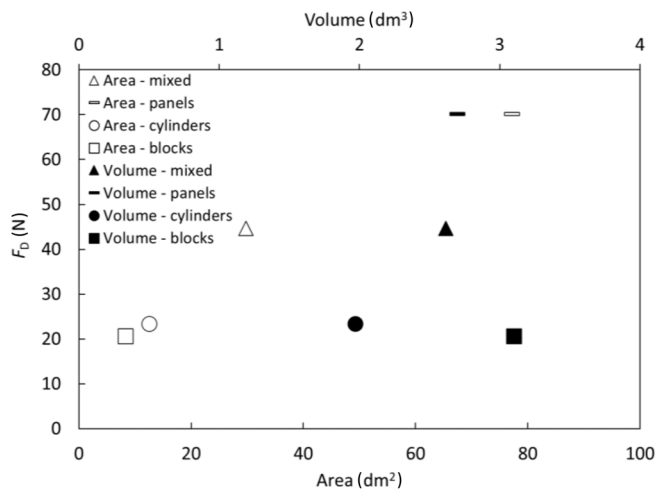
FIGURE 14 Drag force due to debris trapped in the obstacles as a function of both the representative area of the trapped debris and their actual volume.

indicates that for an inundation depth of 4 m, the range of predictions from the Japanese and ASCE design codes range are ~50 to 750 kN/m, in agreement with the inferred values in Figures 13 and 14. The force associated with this type of tsunami has been observed to cause the destruction of a variety of structures (timber buildings and non-structural elements of RC buildings) and shallow-rooted trees (Fraser et al., 2013). Therefore, blockages generating this range of drag force are important to consider in design.

4 | CONCLUSIONS AND RECOMMENDATIONS

In conclusion, these tests have investigated how different debris types interact with an array of obstacles, not previously considered. Setup A considered a debris mix carried by a range of flow rates, whilst Setup B also considered debris types separately but for just one, slightly higher, flow rate. The effect that the debris had on the backwater showed that there were competing factors of debris volume and flow rate, that is, while the available debris for Setup B was only about 40% that of Setup A, the backwater rise was higher, as the upstream flow rate was higher. In Setup B, the panel debris caused the greatest increase in backwater, followed by the mixed, block and cylindrical debris. Dam formation was also affected by debris type and flow rate. Setup A had a random release of debris types, but did show evidence that smaller key logs led to smaller dams and that higher flow rates led to smaller dams. Setup B showed how different debris shapes led to different depths at which key logs formed, with cylindrical debris only becoming keys logs at the

surface, whilst panels formed key logs at a variety of depths. The size of the dam reduced for increasing Froude number. Also, the vertical shape of the dam depended on debris type, with blocks, for example, only producing a free surface dam. For Setup A, there is some evidence of the capture efficiency decreasing with increasing Froude number, expected from the relationship between dam size and flow rate. Setup B showed examples of debris accelerated through partial dams. Drag force on the obstacles and debris was estimated based on the difference in upstream and downstream water levels once the dam was formed. Setup A showed a clear correlation of estimated drag force with Froude number, and results from Setup B showed how debris' shape affects the drag force, with panels experiencing highest drag, followed by mixed debris, cylindrical and blocks the least. It is promising that this important parameter can be estimated using a simple experimental setup.

A limitation of this experiment is that WG1 was constantly hit by debris and had to be covered with a mesh covering to avoid disturbance of the wave gauge. Future tests might consider non-invasive methods to determine the time-varying water depth. On the debris movement, more quantitative data could be obtained by using calibrated video images. Also, different configurations of obstacles, for example, staggered grids, should be considered, as their ability to trap debris could be different. Investigations could be conducted as to the cause of panels being attracted to the flume bed, that is, varying the friction of the bed. Finally, greater numbers of repeat tests would provide more confidence of some of the trends observed.

On the basis of findings in this investigation there are two recommendations that can be made for locations at risk of extreme flooding from storm surges or tsunamis:

1. Since backwater rise is highly sensitive to debris type, consideration must be given to the effects of certain debris types in an inundation zone, that is, for panels that might be designed to fail under particular loads, it would be sensible to design them to break up further, preventing them causing significant blockages and localised increases in water depth, which could otherwise lead to more casualties and increased loads on buildings.
2. The potential for formation of partial dams need to be considered at the scheme design in the inundation zones. This is particularly important where there are rows of structures parallel to the shore and 'corridors' are formed. These might unintentionally lead to accelerated flow which might coincide with evacuation routes.

DATA AVAILABILITY STATEMENT

The data that support the findings of this study are available from the corresponding author upon reasonable request.

ORCID

Piyali Chowdhury https://orcid.org/0000-0001-6294-2552

REFERENCES

Aghl, P. P., Naito, C. J., & Riggs, H. R. (2014). Full-scale experimental study of impact demands resulting from high mass, low velocity debris. *Journal of Structural Engineering*, *140*(5), 11.

Bocchiola, D., Rulli, M. C., & Rosso, R. (2008). A flume experiment on the formation of wood jams in rivers. *Water Resources Research*, *44*(2).

Cinar, G. E., Keen, A., & Lynett, P. (2023). Motion of a debris line source under currents and waves: Experimental study. *Journal of Waterway, Port, Coastal, and Ocean Engineering*, *149*(2), 04022033.

Danielsen, F., Sørensen, M. K., Olwig, M. F., Selvam, V., Parish, F., Burgess, N. D., Hiraishi, T., Karunagaran, V. M., Rasmussen, M. S., Hansen, L. B., Quarto, A., & Suryadiputra, N. (2005). The Asian tsunami: A protective role for coastal vegetation. *Science*, *310*(5748), 643.

Esteban, M., Takagi, H., & Shibayama, T. (Eds.). (2015). *Handbook of coastal disaster mitigation for engineers and planners*. Butterworth-Heinemann.

Fraser, S., Raby, A., Pomonis, A., Goda, K., Chen, S. C., Macabuag, J., Offord, M., Saito, K., & Sammonds, P. (2013). Tsunami damage to coastal defences and buildings in the March 11th, 2011 Mw 9.0 Great East Japan earthquake and tsunami. *Bulletin of Earthquake Engineering*, *11*, 205–239.

Ghobarah, A., Saatcioglu, M., & Nistor, I. (2006). The impact of the 26 December 2004 earthquake and tsunami on structures and infrastructure. *Engineering Structures*, *28*(2), 312–326.

Goseberg, N., Stolle, J., Nistor, I., & Shibayama, T. (2016). Experimental analysis of debris motion due the obstruction from fixed obstacles in tsunami-like flow conditions. *Coastal Engineering*, *118*, 35–49.

Harada, K., & Imamura, F. (2005). Effects of coastal forest on tsunami hazard mitigation—A preliminary investigation. *Tsunamis: Case Studies and Recent Developments*, *23*, 279–292.

Hughes, S. (1993). *Physical models and laboratory techniques in coastal engineering*. World Scientific Publishing Co., Pte. Ltd.

Ikeno, M., Takabatake, D., Kihara, N., Kaida, H., Miyagawa, Y., & Shibayama, A. (2016). Improvement of collision force formula for woody debris by airborne and hydraulic experiments. *Coastal Engineering Journal*, *58*(4), 1640022-1–1640022-23.

Intergovernmental Panel on Climate Change (IPCC). (2014). *Climate change 2014–impacts, adaptation and vulnerability: Regional aspects*. Cambridge University Press.

Kasaei, S., Bryski, E., & Farhadzadeh, A. (2021). Probabilistic analysis of debris motion in steady-state currents for varying initial debris orientation and flow velocity conditions. *Journal of Hydraulic Engineering*, *147*(9), 04021032.

Kennedy, A., Copp, A., Florence, M., Gradel, A., Gurley, K., Janssen, M., Kaihatu, J., Krafft, D., Lynett, P., Owensby, M., Pinelli, J.-P., Prevatt, D. O., Rogers, S., Roueche, D., & Silver, Z. (2020). Hurricane Michael in the area of Mexico beach, Florida. *Journal of Waterway, Port, Coastal, and Ocean Engineering*, *146*(5), 05020004.

Macabuag, J., Raby, A., Pomonis, A., Nistor, I., Wilkinson, S., & Rossetto, T. (2018). Tsunami design procedures for engineered buildings: A critical review. *Proceedings of the Institution of Civil Engineers – Civil Engineering*, *171*, 166–178. https://doi.org/10.1680/jcien.17.00043

Massey, B., & Ward-Smith, J. (1998). *Mechanics of fluids*. Stanley Thornes (Publishers) Ltd.

Mori, N., Takahashi, T., Yasuda, T., & Yanagisawa, H. (2011). Survey of 2011 Tohoku earthquake tsunami inundation and run-up. *Geophysical Research Letters*, *38*, 7.

Naito, C., Cercone, C., Riggs, H. R., & Cox, D. (2014). Procedure for site assessment of the potential for tsunami debris impact. *Journal of Waterway, Port, Coastal, and Ocean Engineering*, *140*, 223–232.

Nistor, I., Goseberg, N., & Stolle, J. (2017). Tsunami-driven debris motion and loads: A critical review. *Frontiers in Built Environment*, *3*.

Park, H., Koh, M. J., Cox, D. T., Alam, M. S., & Shin, S. (2021). Experimental study of debris transport driven by a tsunami-like wave: Application for non-uniform density groups and obstacles. *Coastal Engineering*, *166*, 103867.

Pasha, G. A., & Tanaka, N. (2020). Characteristics of a hydraulic jump formed on upstream vegetation of varying density and thickness. *Journal of Earthquake and Tsunami*, *14*(3).

Raby, A., Macabuag, J., Pomonis, A., Wilkinson, S., & Rossetto, T. (2015). Implications of the 2011 Great East Japan Tsunami on sea defence design. *International Journal of Disaster Risk Reduction*, *14*, 332–346.

Rahman, M. A., Tanaka, N., & Anjum, N. (2022). Damming effects of tsunami-borne washed-out trees in reducing local scouring and tsunami energy behind a coastal embankment. *Applied Ocean Research*, *126*, 103260.

Schmocker, L., & Hager, W. H. (2013). Scale modeling of wooden debris accumulation at a debris rack. *Journal of Hydraulic Engineering*, *139*(8), 827–836.

Stolle, J., Takabatake, T., Mikami, T., Shibayama, T., Goseberg, N., Nistor, I., & Petriu, E. (2017). Experimental investigation of debris-induced loading in tsunami-like flood events. *Geosciences*, *7*(3), 25.

Stolle, J., Takabatake, T., Nistor, I., Mikami, T., Nishizaki, S., Hamano, G., Ishii, H., Shibayama, T., Goseberg, N., & Petriu, E. (2018). Experimental investigation of debris damming loads under transient supercritical flow conditions. *Coastal Engineering*, *139*, 16–31.

Tanaka, N., & Onai, A. (2017). Mitigation of destructive fluid force on buildings due to trapping of floating debris by coastal forest during the Great East Japan tsunami. *Landscape and Ecological Engineering*, *13*(1), 131–144.

Wahl, T., Jain, S., Bender, J., Meyers, S. D., & Luther, M. E. (2015). Increasing risk of compound flooding from storm surge and rainfall for major US cities. *Nature Climate Change*, *5*(12), 1093–1097.

Zscheischler, J., Westra, S., Van Den Hurk, B. J., Seneviratne, S. I., Ward, P. J., Pitman, A., AghaKouchak, A., Bresch, D. N., Leonard, M., Wahl, T., & Zhang, X. (2018). Future climate risk from compound events. *Nature Climate Change*, *8*(6), 469–477.

APPENDIX A

FIGURE A1 Overhead and side view of the dam formation for mixed group repeat no. 2.